Available online at www.sciencedirect.com
ScienceDirect
Astroparticle Physics 26 (2006) 111–118
Astroparticle Physics
www.elsevier.com/locate/astropart

The electron–hadron separation performance of the PAMELA electromagnetic calorimeter

M. Boezio [b], M. Pearce [a,*], M. Albi [b,c], V. Bonvicini [b], J. Lund [a], J. Lundquist [b], E. Mocchiutti [b], A. Vacchi [b], G. Zampa [b], N. Zampa [b]

[a] The Royal Institute of Technology (KTH), Department of Physics, Albanova University Centre, 10691 Stockholm, Sweden
[b] INFN Sezione di Trieste, Padriciano 99, 34012 Trieste, Italy
[c] Dipartimento di Astronomia dell'Universitá di Trieste, via G.B. Tiepolo 11, 34131 Trieste, Italy

Received 7 March 2006; received in revised form 10 May 2006; accepted 20 May 2006
Available online 21 June 2006

Abstract

A silicon-tungsten sampling imaging calorimeter has been designed and built for the PAMELA satellite-borne experiment. The main physics goals of the experiment are the measurement of the flux of antiprotons (80 MeV–190 GeV) and positrons (50 MeV–270 GeV) in the cosmic radiation. The calorimeter has been designed to identify antiprotons from an electron background and positrons in a background of protons with a high efficiency and rejection power. This work presents the electron–hadron separation capabilities of the calorimeter as obtained using both Monte Carlo and test beam data. The calorimeter is found to have sufficient performance to reach the primary scientific objectives of PAMELA, providing a proton rejection factor of $\sim 10^5$ while keeping a $\sim$90% efficiency in selecting electrons and positrons. From simulations, an electron rejection factor of $\sim 10^5$ in antiproton measurements ($\sim$90% antiproton identification efficiency) is demonstrated.

Keywords: PAMELA; Cosmic rays; Silicon-tungsten calorimeter; Electron; Hadron

1. Introduction

The PAMELA apparatus [1] (a Payload for Antimatter Matter Exploration and Light-nuclei Astrophysics) is a satellite-borne experiment which is primarily designed to study antiparticles (antiprotons and positrons) in the cosmic radiation. PAMELA is housed on-board a Resurs-DK1 earth-observation satellite that is scheduled to be launched in 2006. The satellite orbit is elliptical and semi-polar, with an altitude varying between 350 and 600 km, at an inclination of 70.4°. The mission is foreseen to last for at least three years.

An accurate determination of the antiproton and positron energy spectra allows cosmic ray propagation [2] and solar modulation [3] to be studied. Antiparticles could also be produced from exotic sources such as primordial black holes [4] or the annihilation of supersymmetric [5] or Kaluza-Klein [6] dark matter particles. Almost all contemporary cosmic ray antiparticle data have been obtained by balloon-borne experiments. Recent measurements for antiprotons include BESS00 [7], AMS [8] and CAPRICE98 [9]; and recent positron measurements include AMS [10], CAPRICE98 [11] and HEAT00 [12].

The data-taking time (usually $\sim$24 h) and the presence of a residual overburden of atmosphere ($\sim$5 g/cm^2) limit the accuracy of these measurements. PAMELA will determine the flux of antiprotons (order of 10^4), (80 MeV–190 GeV) and positrons (order of 10^5), (50 MeV–270 GeV) in the cosmic radiation across a wide energy

* Corresponding author. Tel.: +46 855378183; fax: +46 855378216.
E-mail address: pearce@particle.kth.se (M. Pearce).

0927-6505/$ - see front matter © 2006 Elsevier B.V. All rights reserved.
doi:10.1016/j.astropartphys.2006.05.005

range and with unprecedented statistics. The measurements are complicated by the substantial background from protons (for the positron flux) and electrons (in the case of antiprotons). The ability of the PAMELA electromagnetic calorimeter to separate electrons[1] from hadrons has been studied using particle beam tests and Monte Carlo simulations. The results are presented in this paper.

In the next section, the PAMELA experiment is described with particular attention paid to the electromagnetic calorimeter. In Section 3, the electron–hadron separation method is described. In Section 4 the simulations and tests at particle beams used to assess the electron–hadron separation performance are described. The results from these studies are presented in Section 5 and are discussed in the context of the in-orbit performance of the calorimeter in Section 6. Finally, conclusions are presented in Section 7.

2. The PAMELA experiment

The layout of the PAMELA experiment is detailed in Fig. 1. PAMELA is built around a 0.43 T permanent magnet spectrometer ('tracker') equipped with six planes of 300 μm thick double-sided silicon detectors allowing the sign, absolute value of charge and momentum of traversing charged particles to be determined [13]. The acceptance of the tracker (which also defines the overall acceptance of the PAMELA experiment) is 21.5 cm^2sr and the maximum detectable rigidity is ~1 TV. The limited tracking resolution causes a fraction of high momentum particles, i.e. with low deflection, to be reconstructed with the wrong curvature. Thus, they are assigned the wrong sign of the charge (spillover effect). Since there are many more protons than antiprotons and relatively more electrons than positrons, spillover effects limit the upper detectable antiparticle momentum to ~190 GeV/c (~270 GeV/c) for antiprotons (positrons). The tracker is surrounded by a plastic scintillator veto shield [14]. An electromagnetic calorimeter mounted below the tracker measures the energy of incident electrons and allows topological discrimination between electromagnetic and hadronic showers (or non-interacting particles). This discriminatory ability is the focus of this paper. The calorimeter is described more fully in Section 2.1. Planes of plastic scintillator mounted above and below the tracker form a time-of-flight system which also provides the primary experimental trigger [15]. The timing resolution of the time-of-flight system is ~300 ps which allows albedo particles to be rejected at the 60 sigma level. Proton-electron separation is also possible below ~1 GeV/c. Ionising energy loss measurements allow an estimation of the absolute charge of particles selected by the time-of-flight system as down-going. The volume between the upper two time-of-flight planes is bounded by an additional plastic scintillator anticoincidence system. A plastic scintillator system mounted beneath the calorimeter provides an additional stand-alone trigger for high energy electrons and is followed by a neutron detection system comprising ^{3}He-filled tubes within a polyethylene moderator for the selection of very high energy electrons and positrons (up to 3 TeV) which shower in the calorimeter but do not necessarily pass through the spectrometer.

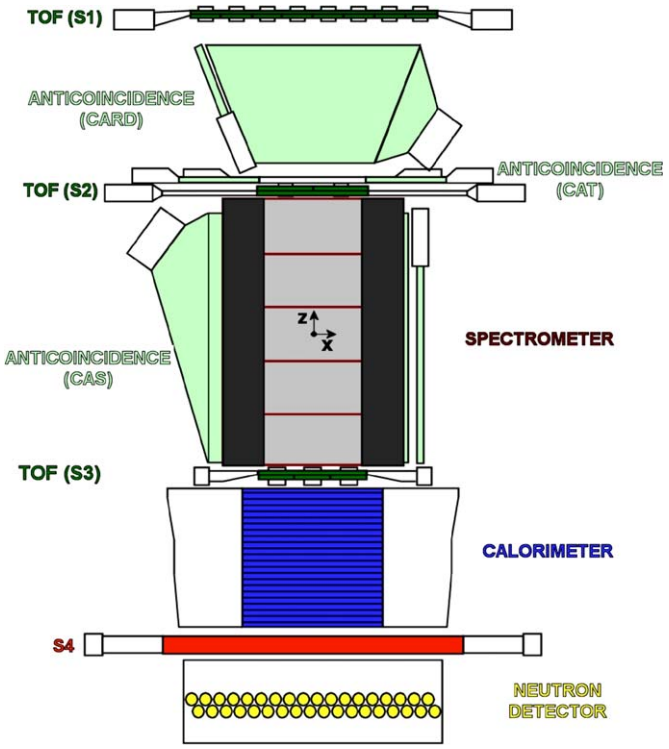

Fig. 1. A schematic overview of the PAMELA satellite experiment. The experiment stands ~1.2 m high and, from top to bottom, consists of a time-of-flight (ToF) system (S1, S2, S3 scintillator planes), an anticoincidence shield system, a permanent magnet spectrometer (the magnetic field runs in the y-direction), a silicon-tungsten electromagnetic calorimeter, a shower tail scintillator (S4) and a neutron detector. The experiment has an overall mass of 450 kg. The origin of the PAMELA coordinate system is located at the centre of the tracking system. The x-axis runs to the right, parallel to the silicon planes in the spectrometer, the y-axis points into the page, and the z-axis is orientated vertically.

2.1. The electromagnetic calorimeter

The sampling electromagnetic calorimeter comprises 44 single-sided silicon sensor planes (380 μm thick) interleaved with 22 plates of tungsten absorber [16]. Each tungsten layer has a thickness of 0.26 cm, which corresponds to 0.74 X_0 (radiation lengths), giving a total depth of 16.3 X_0 (~0.6 nuclear interaction lengths). Each tungsten plate is sandwiched between two printed circuit boards upon which the silicon detectors and associated read-out electronics are mounted. The 8×8 cm^2 silicon detectors are segmented into 32 read-out strips with a pitch of 2.4 mm. The silicon detectors are arranged in a 3×3 matrix and each of the 32 strips is bonded to the corresponding strip

[1] The term electron also refers to positrons, unless specifically stated otherwise.

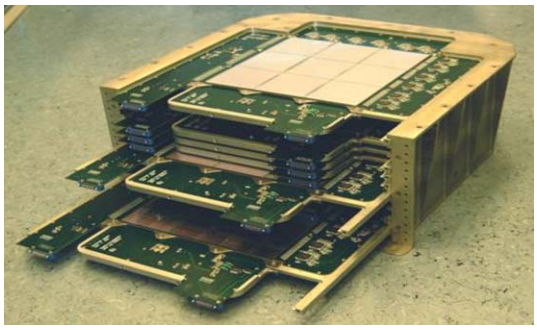

Fig. 2. The PAMELA electromagnetic calorimeter partially equipped with silicon and tungsten planes. The device is ~20 cm tall and the active silicon layer is $\sim 24 \times 24\ \mathrm{cm}^2$ in cross-section. Some of the circuit boards upon which the silicon detectors are mounted are partially extracted.

on the other two detectors in the same row (or column), thereby forming 24 cm long read-out strips. The orientation of the strips of two consecutive layers is orthogonal and therefore provides two-dimensional spatial information ('views'). Fig. 2 shows the calorimeter prior to integration with the other PAMELA detectors. As well as providing a means to distinguish between electrons and hadrons, the calorimeter reconstructs the energy of incident electrons independently from the tracking system, allowing a cross-calibration between the two methods. The constant term for the calorimeter energy resolution has been measured as ~5.5% for electromagnetic showers generated by particles entering the calorimeter within the acceptance of the tracking system up to an energy of several hundred GeV.

3. Electron–hadron separation

Protons and electrons dominate the positively and negatively charged components of the cosmic radiation, respectively. One of the main tasks of the calorimeter is to select positrons and antiprotons from like-charged backgrounds which are significantly more abundant. Positrons must be identified from a background of protons that increases from about 10^3 times the positron component at 1 GeV/c to $\sim 5 \times 10^3$ at 10 GeV/c and antiprotons from a background of electrons that decreases from $\sim 5 \times 10^3$ times the antiproton component at 1 GeV/c to less than 10^2 times above 10 GeV/c. This means that the PAMELA system must separate electrons from hadrons at a level of 10^5–10^6. Much of this separation must be provided by the calorimeter, i.e. electrons must be selected with an acceptable efficiency and with as small a hadron contamination as possible.

The main stages for the identification of electrons and antiprotons are as follows. The time-of-flight system is used to select down-going singly-charged particles (proton-electron separation is possible below ~1 GeV/c). Information from the tracker is then used to determine the sign of charge and rigidity (momentum/charge) over a wide range of momenta (~50 MeV/c to ~1 TeV/c). Finally, the longitudinal and transverse segmentation of the calorimeter, combined with the measurement of the particle energy loss in each silicon strip, allows a high identification (or rejection) power for electromagnetic showers. Electromagnetic and hadronic showers differ in their spatial development and energy distribution in a way that can be distinguished by the calorimeter. This is demonstrated in Fig. 3 which shows examples of an electromagnetic shower induced by an electron (left) and an interacting proton (right), recorded during tests with particle beams at the CERN SpS facility. All incident particles have a momentum of 50 GeV/c.

The use of a simple variable, such as the total energy deposited in the calorimeter, allows an effective separation between electrons and hadrons. For incident hadrons of a given energy, the distribution of total energy deposited in the calorimeter is essentially flat with a sharp peak at low energies for non-interacting hadrons. For electrons, the total energy deposited in the calorimeter for a given incident energy is normally distributed, as long as most of the shower is contained. For higher electron energies, a tail to low energies can, however, decrease the efficiency for electron identification. The use of this variable is illustrated in Fig. 4 where the total energy deposited by 67504 protons and 3342 electrons at 50 GeV/c of momentum are shown. After a cut placed at 7300 mip (where 1 mip is the energy deposited by a minimum ionising particle) 14 protons (99.98% reduction) and 3197 electrons (4.3% reduction) remain.

Additional variables have been used to further separate electromagnetic and hadronic showers in the calorimeter. Several of these variables rely on the derivation of the shower axis. Where possible the shower axis is defined using tracking information from the tracking system. When this is not possible because (e.g.) the tracker was not present during the beam tests, the following procedure is adopted. The 22 silicon planes in each view are divided into strips. The impact point within the ith plane is defined as the centre of gravity, $\bar{x}$, of the measured energies, E_i (>0.7 mip) deposited in strips with co-ordinates x_i, where $\bar{x} = \frac{\sum_i x_i E_i}{\sum_i E_i}$. When this procedure is performed at several depths in the calorimeter, the shower axis can be determined by a linear fitting procedure to an accuracy of a few mm. In flight, the shower axis will be determined using tracking information from the spectrometer with an expected 10^3 improvement in accuracy. In the following sections each of the additional variables used to distinguish between electron and hadron interactions are described in detail.

3.1. The starting point of the shower

There is a high probability (>89%) that an electromagnetic shower will start in the first 3 planes of the calorimeter. For hadronic showers, the starting point is distributed more uniformly. The variable $R = \sum_{j=1}^{2} \sum_{i=1}^{22} \theta_{ij} \cdot i$, is formed as a sum over the 22 calorimeter planes which each contain 2

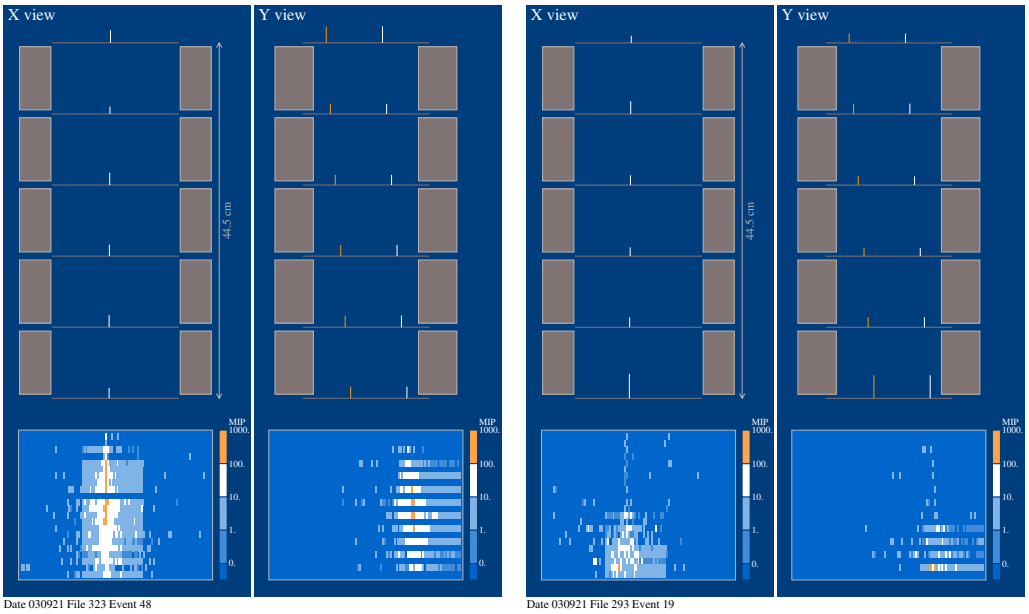

Fig. 3. An event display of a 50 GeV/c electron (left) and proton (right) recorded at CERN SpS facility. In the top part of the figure both views (X-left, Y-right) of the six silicon planes are shown inside the magnetic cavity (field lines in the *Y*-direction). Hits in the tracking system are shown (including ambiguities for the Y-view). In the bottom part of the figure, the two views (X and Y) of the calorimeter are shown. The colour scale indicates the detected energy in each strip (from dark (blue in webversion) none, to light (orange in webversion), greater than 100 mip). The topological and energetic differences between electromagnetic and hadronic showers can be clearly seen. Signals from the odd planes of the Y-view of the calorimeter were not read out during this test. One of the X-view planes was also not operational and was later replaced.

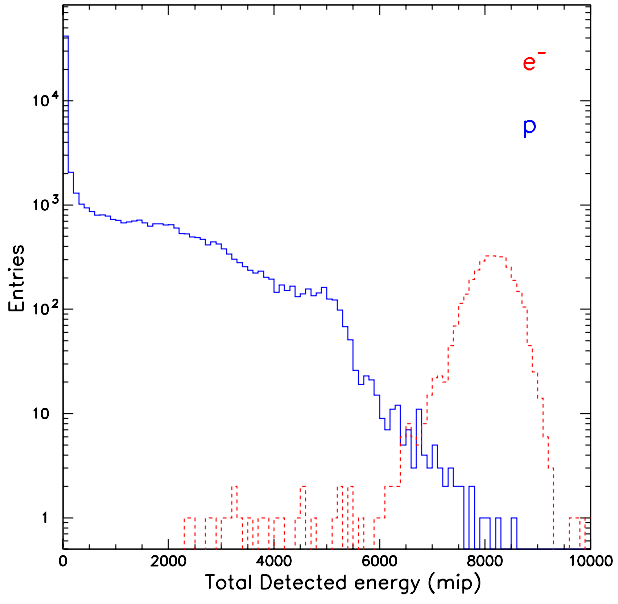

Fig. 4. An illustration of electron–proton separation using a simple total deposited energy variable. The test beam data were collected for particles of momentum 50 GeV/c. After a cut placed at 7300 mip 14 protons (99.98% reduction) and 3197 electrons (4.3% reduction) remain.

orthogonal views and $\theta_{ij} = 1$ if the ith plane of the jth view has strips registering energies compatible with a minimum ionising particle within 4 mm from the reconstructed shower axis. If this condition is not fulfilled then $\theta_{ij} = 0$. For electromagnetic showers, R assumes low values, while for a non- or partially-interacting hadron, R takes higher values. Another variable which is sensitive to the starting point of the shower is the energy deposited in a cylinder of diameter four times the Molière radius (R_m) for tungsten (8 silicon strips) evaluated for the first 3 calorimeter planes.

3.2. The longitudinal shower profile

The energy deposited in an electromagnetic shower significantly decreases and spatially broadens after the shower maximum. The location of the maximum is derived using the momentum of the particle derived by the tracking system or by the beam set-up. For a hadronic shower, energy is deposited approximately uniformly and any maximum lies deeper in the calorimeter for a given incident energy. The longitudinal shower profile is assessed by determining what fraction of the total deposited energy lies at least five planes after the expected electromagnetic shower maximum. Another variable sensitive to the longitudinal shower profile is the amount of energy deposited in the last four calorimeter planes within a cylinder of radius $2R_m$. This variable assumes a lower value for electromagnetic showers where the shower maximum is usually contained within the calorimeter. The maximum energy detected in a single strip can also be used. For hadronic events this can be very large if (e.g.) a silicon nucleus is fragmented.

3.3. The transverse shower profile

The transverse shower profile is evaluated through the amount of energy deposited per strip inside a cylinder of

radius $2R_m$ centred on the reconstructed shower axis. For electrons, ~95% of the deposited energy should fall within the cylinder. This is a potentially powerful way to separate electrons and hadrons but requires a reliable definition of the shower axis. This selection is therefore likely to be more performant in flight when the tracker can be used to define the shower axis.

3.4. The topological development of the shower

For electromagnetic showers, the shower particle multiplicity is expected to increase with calorimeter depth up to the shower maximum. Furthermore, the shower particles should be collimated along the shower axis. A variable exploiting this behaviour is defined as $\sum_{j=1}^{2}\sum_{i=1}^{pl_{max}} n_{hit}(i,j)\cdot i$, where n_{hit} is the number of hit strips in the jth view of plane i within a cylinder of radius $2R_m$ centred on the shower axis. The sum over planes is truncated at the calculated electromagnetic shower maximum for a given incident energy, pl_{max}, for a given incident energy provided by either the tracking system or by the beam set-up. For electromagnetic (hadronic) showers this variable assumes high (low) values.

4. Particle beam tests and simulations

The electron–hadron separation of the calorimeter has been evaluated using data from tests with particle beams at CERN and Monte Carlo simulations. There are two aims to this study. The first is to estimate the calorimeter's hadron rejection capability and electron selection efficiency. The second is a comparison between test beam and simulation results which can be used to validate simulation studies of the calorimeter in situations resembling those expected in orbit, as discussed in Section 6.

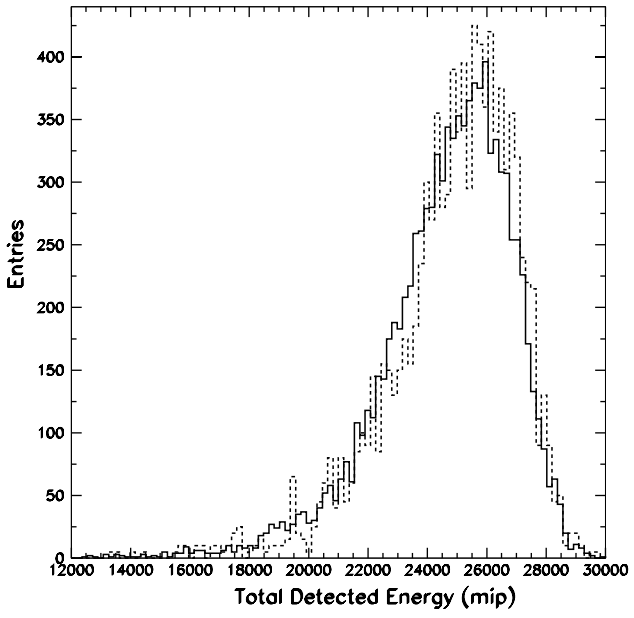

Fig. 5. The total energy deposited in the calorimeter, recorded for electrons of momentum 200 GeV/c. Data are shown as a solid line while simulations are shown as a dashed line.

The test beam data used in the analyses were collected at three different occasions at the CERN PS and SPS test beam facilities during 2002 and 2003. In each test, the calorimeter was equipped with approximately half of the total number of silicon planes. The performance results presented in the next section are therefore conservative. Monte Carlo simulations of the calorimeter performance used the GEANT framework, version 3.21 [17]. The default GHEISHA hadron shower package was used to simulate the interactions of hadrons with the nuclei of the matter traversed. The incident particle beams were assumed to be monoenergetic and contamination free. The validity of these assumptions is further discussed in [18]. The simulation was found to reproduce the data well. This is demonstrated in Fig. 5 which shows the total energy deposited in the calorimeter for electrons of momentum 200 GeV/c for both test beam data and simulations.

5. Results

Combinations of the variables described in Section 3 were used to provide electron–hadron separation at a given incident particle energy. The selections were optimised using only the data collected during particle beam tests. Monte Carlo simulations were not used for this purpose. The complete set of selections used for each incident particle energy is listed elsewhere [18]. As an example, a selection based on the topological variable described in Section 3.4 is applied to the 3197 electrons and 14 protons remaining after the simple total energy cut described in Fig. 4. After this selection is performed, 3116 electrons (2.5% reduction) and 7 protons (50% reduction) remain, as shown in Fig. 6.

Fig. 7 shows the efficiency (upper panel) and contamination (lower panel) of the final electron selection as a function of momentum. The full circles represent test beam data and the open squares represent simulated data. When tuning the data selections, the electron efficiency was kept above 90% where-ever possible. The agreement between simulation and experimental data is acceptable. In the lower panel of Fig. 7 the proton contamination is shown as a function of momentum for both beam test data (full circles) and simulated data (open squares). The arrows show the 68% confidence levels if no events survived the selection. The data points at 3 and 10 GeV/c are for electron/pion separation and therefore do not directly apply to the electron/proton separation study because pions with a momentum of 3 GeV/c have ~1 GeV more kinetic energy that can be deposited in the calorimeter, than protons of the same momentum. This will result in a higher contamination for pions compared to protons. However, the pion data can usefully be used to compare simulation and beam test results. Good agreement between simulations and beam test data can be seen. Fluctuations in the measured

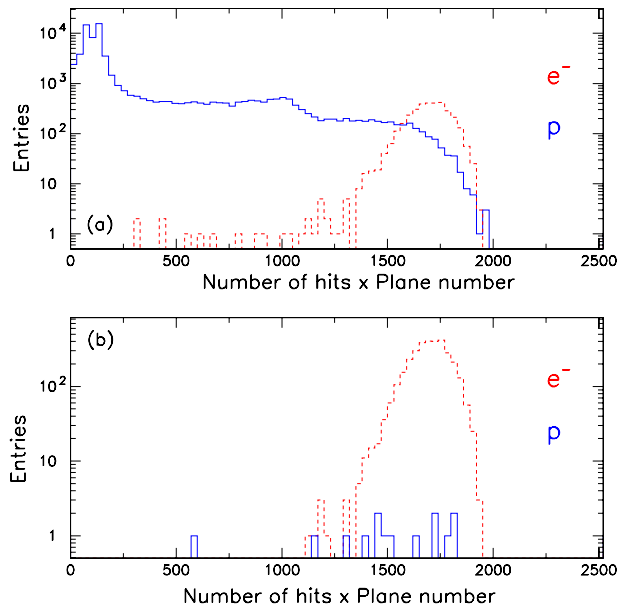

Fig. 6. The upper panel shows the topological variable ('number of hits × plane number') described in Section 3.4 for the same 67504 protons and 3342 electrons as shown in Fig. 4. In the lower panel, the events remaining after a total energy cut at 7300 mip are shown, corresponding to 3197 electrons and 14 protons. A further cut on the topological variable at 1500 leaves 3116 electrons (2.5% reduction) and 7 protons (50% reduction).

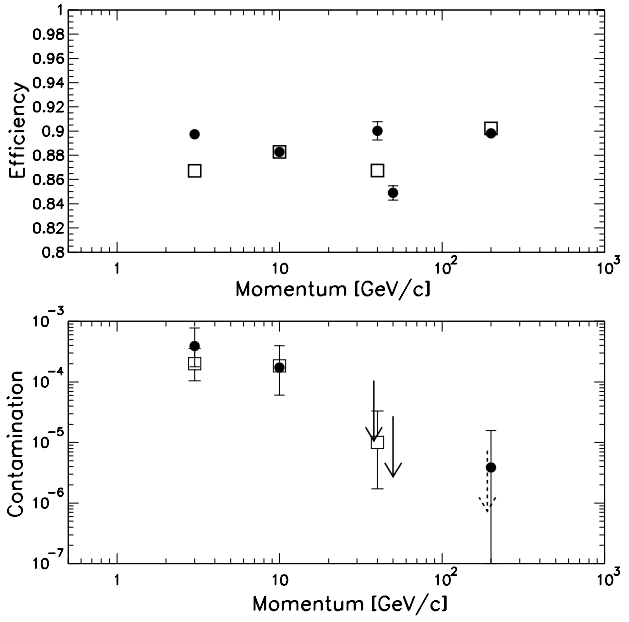

Fig. 7. *Upper panel*: The electron identification efficiency, shown as a function of incident particle momentum. The full circles and open squares represent beam test and simulated data, respectively. *Lower panel*: The proton contamination in the electron selection, shown as a function of incident particle momentum. The full circles and open squares represent beam test and simulated data, respectively. The arrows indicate the 68% confidence level for test beam data if no events survive the selection. The dashed arrow is for simulated protons at 200 GeV/c. The data at 10, 40 and 200 GeV/c are displaced for clarity.

efficiencies as a function of energy are due to different calorimeter configurations (i.e. number of planes equipped and read out [18]), energy dependent selections and different beam conditions (direction and impact point on the calorimeter). These results refer to a partially equipped calorimeter and should be considered as lower limits of the calorimeter performance.

6. Discussion

In this section the scientific results achievable with the PAMELA experiment employing its calorimeter as a positron and antiproton identifier are discussed. As shown in the previous section, results obtained from test beam data indicate that even with a partially equipped calorimeter it is possible to achieve a proton rejection factor of at least 10^{-5} above 10 GeV/c while maintaining an electron selection efficiency of ~90%. Furthermore, a good agreement is found between simulated and experimental calorimeter data. Therefore, simulation tools have been used to study the in-orbit performance of the calorimeter. The simulation employed the GPAMELA code [19] that reproduces the entire PAMELA geometry and component detectors.

Proton, positron, electron and antiproton energy spectra were simulated using published particle fluxes [5,20,21] assuming pure secondary production during cosmic-ray propagation in the galaxy for positrons and antiprotons. The fluxes were simulated for momenta above 1 GeV/c since at lower momenta a clean separation between protons/positrons and antiprotons/electrons is provided by the velocity and ionization losses measured by the ToF system, as verified using ground data cosmic rays. An isotropic distribution of down-going particles were simulated above PAMELA and events were saved for further study if a 'trigger' was generated, i.e. coincidental signals in the three layers of ToF scintillators. Only singly-charged particles identified by the ToF scintillators were used for the calorimeter studies. The particle direction and momentum derived by the tracking system was also used with the calorimeter information. The momentum information was smeared according to the experimental momentum resolution (0.001 GV^{-1}). Positrons were identified with the calorimeter as described in the previous sections and antiprotons were identified by selecting electromagnetic showers in the calorimeter with the highest possible efficiency and then rejecting them.

Fig. 8 shows the results of these analyses for positrons. The filled circles indicate the expected PAMELA performance for a pure secondary positron component (solid line, from [21]). Statistical errors accounting for the calorimeter selection efficiency and a three year long mission are included in the expected PAMELA data. The data are multiplied by $p^{2.7}$ (where p is momentum) for clarity.[2] As well as the expected positron spectrum, the figure also shows the proton component. The dotted line indicates

[2] The fluxes are presented in momentum units since the selection conditions are momentum based, with the momentum (rigidity) determined by the tracking system.

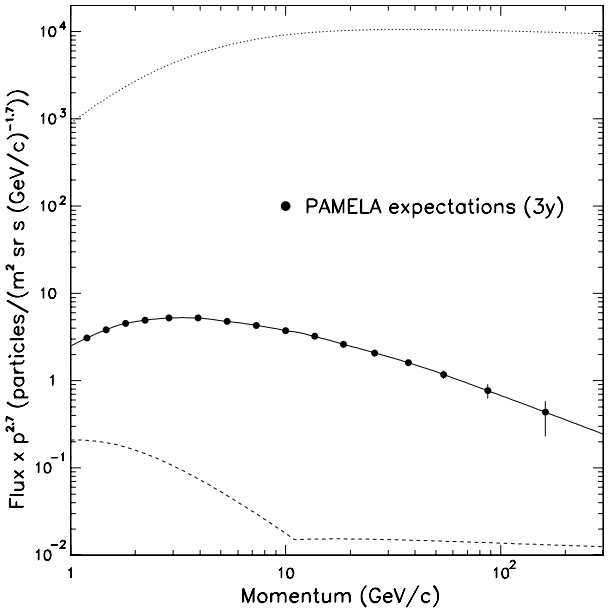

Fig. 8. The PAMELA calorimeter in-orbit identification performance for positrons. The solid line represents the cosmic-ray positron spectrum for a pure secondary origin [21]; the dotted line represents the cosmic-ray proton spectrum (from [20]); the dashed line represents the spectrum of protons surviving the calorimeter positron selection. The expected PAMELA performance for a pure secondary component (filled circles) is also indicated together with statistical errors.

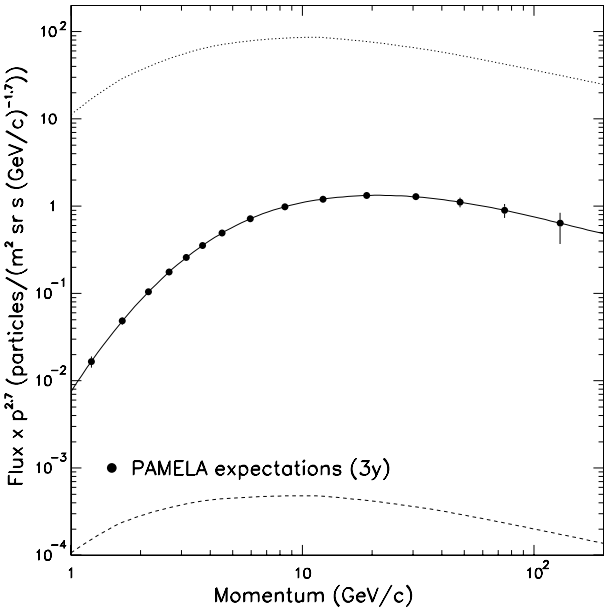

Fig. 9. The PAMELA calorimeter in-orbit identification performance for antiprotons. The solid line represents the cosmic-ray antiproton spectrum for a pure secondary origin [5]; the dotted line represents the cosmic-ray electron spectrum (from [21]); the dashed line represents the spectrum of electrons surviving the calorimeter antiproton selection. The expected PAMELA performance for a pure secondary component (filled circles) is indicated. Only statistical errors are included for the expected PAMELA data.

the cosmic-ray proton spectrum (from [20]) clearly showing the background level for the positron analysis. The dashed line shows the spectrum of protons which survives the calorimeter positron selection. The surviving protons account for ~9% of the positron flux at 1 GeV/c, decreasing to below 5% above 1.5 GeV/c and flattening out to below 2% above 3 GeV/c.

Similarly, Fig. 9 shows the expected PAMELA performance for a pure secondary antiproton component (solid line, from [5]) along with the electron spectrum before (dotted line, from [21]) and after (dashed line) the calorimeter antiproton selection. After selection electrons account for less than 2% of the antiproton flux at 1 GeV/c and this decreases to below 1% above 1.5 GeV/c.

It should be noted that below ~2 GeV/c additional proton/electron rejection power is provided by the ToF system and above ~10 GeV/c by the neutron detector.

7. Conclusions

The PAMELA calorimeter has been extensively tested at particle beam facilities and studied with simulations. Combining these data, the electron/hadron separation performance of the calorimeter has been determined. It has been shown that the PAMELA calorimeter is able to identify the rare antiproton and positron components in the cosmic radiation with a background at the percent level and lower, especially at scientifically interesting momenta >10 GeV/c.

Acknowledgements

The authors thank the PAMELA Collaboration for their support during the writing of this paper. In particular, we would like to acknowledge Francesco Cafagna and Marialuigia Ambriola for their help with the PAMELA simulation package, GPAMELA; Francesca Volpe for her help in setting up simulation codes; and Elena Vannuccini for her help with the tracker data. The KTH group thanks The Swedish National Space Board (Rymdstyrelsen) and The Swedish Research Council (Vetenskapsrådet) for financial support.

References

[1] M. Boezio, The PAMELA space experiment, in: Proceedings of the 29th International Cosmic Ray Conference, Pune, India, 2005. Available from: <http://wizard.roma2.infn.it/pamela>.
[2] See for example: I.V. Moskalenko et al., ApJ. 586 (2003) 1050.
[3] See for example: Y. Asaoka et al., Phys. Rev. Lett. 88 (2002) 051101.
[4] K. Maki et al., Phys. Rev. Lett. 76 (1996) 3474.
[5] L. Bergström et al., Phys. Rev. D. 59 (1999) 43506.
[6] D. Hooper et al., Phys. Rev. D. 71 (2005) 083503.
[7] Y. Asaoka et al., Phys. Rev. Lett. 88 (2002) 051101. Available from: <astro-ph/0109007>.
[8] M. Aguilar et al., Phys. Rept. 366 (2002) 331.
[9] M. Boezio et al., Astrophys. J. 561 (2001) 787. Available from: <astro-ph/0103513>.
[10] J. Alcaraz et al., Phys. Lett. B 484 (2000) 10.
[11] M. Boezio et al., Adv. Space Res. 27 (2001) 669.

[12] J.J. Beatty et al., Phys. Rev. Lett. 93 (2004) 241102, astro-ph/0412230.
[13] A. Adriani et al., Nucl. Instr. and Meth. A 511 (2003) 72.
[14] S. Orsi et al., Adv. Space Res. 37 (10) (2006) 1853–1856.
[15] G. Osteria et al., Nucl. Instr. and Meth. A 535 (2004) 152.
[16] M. Boezio et al., Nucl. Instr. and Meth. A 487 (2002) 407.
[17] R. Brun et al., Detector description and simulation tool, CERN Program Library (1994).
[18] J. Lund, Antiparticle identification studies for the PAMELA satellite experiment', PhD thesis, KTH, Stockholm, 2004. Available from: <http://www.particle.kth.se>.
[19] GPAMELA simulation code homepage: http://www.ba.infn.it/~ambriola/gpamela/.
[20] T.K. Gaisser et al., in: Proceedings of the 27th International Cosmic Ray Conference, Hamburg, Germany, vol. 5, p. 1643, 2001.
[21] I.V. Moskalenko, A.W. Strong, Astrophys. J. 493 (1998) 694.